RSC Applied Interfaces

ROYAL SOCIETY OF CHEMISTRY

PAPER

View Article Online
View Journal

Cite this: DOI: 10.1039/d5lf00409h

Bifunctional $NaGdF_4$:Yb^{3+}/Er^{3+} upconversion nanoparticles for efficient overall water splitting

Soumantika Jana,[a] Debika Gogoi,[a] Neha Patel,[a] Bo-Yan Feng,[b] Jeffrey C. S. Wu *[b] and Rakesh K. Sharma *[a]

Received 28th December 2025,
Accepted 17th March 2026

DOI: 10.1039/d5lf00409h

rsc.li/RSCApplInter

The development of efficient and robust catalysts for overall water splitting is vital for the advancement of hydrogen-based renewable energy systems. This work reports the synthesis of β-$NaGdF_4$:Yb^{3+}/Er^{3+} upconversion nanoparticles (UCNPs) *via* a solvothermal method and demonstrates their bifunctional catalytic activities toward both the hydrogen evolution reaction (HER) and the oxygen evolution reaction (OER), as well as photoelectrochemical (PEC) water splitting. Electrochemical studies reveal that the UCNPs exhibit low overpotentials and high exchange current density with favorable Tafel slopes for both HER and OER, combined with excellent charge-transfer properties and abundant active sites. Especially, under irradiation, the UCNPs exhibit enhanced PEC activities, benefiting from their strong light–matter interactions and photon upconversion capability, which facilitates the absorption of near-infrared photons and converts them into visible emission, thereby enhancing charge carrier dynamics. The bifunctional $NaGdF_4$:Yb^{3+}/Er^{3+} electrodes also attain efficient overall water splitting, requiring ~1.52 V to reach 10 mA cm^{-2} under simulated solar irradiation with remarkable stability over 24 h. To the best of our knowledge, this is the first demonstration of $NaGdF_4$:Yb^{3+}/Er^{3+} UCNPs acting as a bifunctional catalyst for electrochemical and photoelectrochemical overall water splitting, offering new avenues toward full-spectrum solar energy harvesting and sustainable hydrogen production.

1. Introduction

Green hydrogen, known as a clean and sustainable energy carrier, holds vast potential for transforming the global energy landscape and driving sustainable development. Among the different production strategies, photocatalytic water splitting offers a fully carbon-free route for hydrogen generation; however, its efficiency remains far lower than that of electrocatalytic methods.[1,2] To address this challenge, photoelectrocatalytic (PEC) water splitting has emerged as a promising approach, effectively combining the advantages of photocatalysis and electrocatalysis to improve overall hydrogen production efficiency.[2,3] Water, due to its abundance and non-toxic nature, has long been explored for a variety of applications. In the energy domain, hydrogen derived from water splitting is regarded as a vital alternative fuel for building a clean, renewable, and sustainable energy infrastructure. Nevertheless, water splitting is a thermodynamically uphill reaction that requires external energy input. The process proceeds through two half-cell reactions: the hydrogen evolution reaction (HER) and the oxygen evolution reaction (OER). Of these, OER is more energy-intensive, involving a complex four-electron transfer mechanism and exhibiting sluggish kinetics compared to HER.[4,5] To lower the energy barrier and enhance efficiency, researchers have developed a wide range of catalytic materials.[6–8] These catalysts have been designed to function as photocatalysts, electrocatalysts, or photoelectrocatalysts for driving HER and OER. Despite significant progress, the performance of most reported catalysts still falls short of the benchmark set by noble-metal-based electrocatalysts. Consequently, the development of highly efficient, stable, and cost-effective alternatives remains a key research priority.[9–12] To further enhance photocatalyst performance, it is crucial to develop materials capable of effectively utilizing the entire solar spectrum. Since nearly 43% of solar energy lies in the near-infrared (NIR) region, tapping into this part of the spectrum can markedly enhance photocatalytic performance. In this regard, upconversion nanoparticles (UCNPs) have attracted significant attention, as they can absorb multiple low-energy NIR photons and convert them into higher-energy visible or ultraviolet emissions. This photon upconversion ability broadens the absorption profile of photocatalysts, leading to enhanced charge carrier generation and improved photoelectrochemical (PEC) efficiency. Among various UCNPs, β-$NaGdF_4$ has emerged as a

[a] *Sustainable Materials and Catalysis Research Lab, IIT Jodhpur, Rajasthan 342030, India. E-mail: rks@iitj.ac.in*
[b] *Department of Chemical Engineering, National Taiwan University, Taipei 10617, Taiwan. E-mail: cswu@ntu.edu.tw*

favourable candidate for co-doping with lanthanide ion pairs such as Yb^{3+}/Er^{3+} and Yb^{3+}/Tm^{3+}, owing to its robust photochemical stability and low phonon energy.[13–15] Consequently, constructing hybrid photocatalysts that couple lanthanide-doped UCNPs with visible-light-active semiconductors is a promising strategy for maximizing solar energy harvesting. Several such full-spectrum-responsive systems have been reported, including $NaGdF_4:Yb^{3+}$, $Er^{3+}@BiFeO_3$,[15] $NaGdF_4:Yb^{3+},Tm^{3+}@TiO_2$,[16,17] $NaGdF_4:Yb:Er/Ag/TiO_2$,[18] $NaYF_4:Yb^{3+},Gd^{3+},Tm^{3+}@Bi_2WO_6$,[19] Yb^{3+},Er^{3+} co-doped $NaGdF_4/BiVO_4$ embedded Cu_2O,[20] $NaGdF_4:Yb,Tm@ZnO/Ag_3PO_4$,[21] *etc.*, where researchers have utilized these materials mostly as photocatalysts for various dye degradation, water purification, antibacterial wound healing, photoelectrochemical water reduction, cancer biomarkers, *etc.* Yet, despite the advances, the dual functionality of these UCNPs as both electrocatalysts and photocatalysts remains largely unexplored, highlighting an important direction for future investigation. Hence, in this study, we present the preparation and utilization of $NaGdF_4$ UCNPs doped with Yb^{3+} and Er^{3+} for both electrochemical and photoelectrochemical water-splitting processes. Initially, their catalytic activity toward the hydrogen and oxygen evolution reactions was examined. Subsequently, photoelectrocatalytic HER and OER measurements were performed. The findings reveal that these UCNPs exhibit remarkable potential for solar-driven water splitting, and further investigations are underway to expand this work. This study explores a compositionally simple lanthanide fluoride UCNP as a bifunctional platform capable of operating under both electrochemical and photoelectrochemical water-splitting conditions, highlighting an alternative design strategy distinct from conventional semiconductor-coupled systems.

2. Experimental section

2.1. Synthesis of the UCNPs

$NaGdF_4$ doped with Yb^{3+}/Er^{3+} ($NaGdF_4:Yb^{3+}/Er^{3+}$) was prepared using a modified single-step solvothermal route. In a typical process, 1.36 mmol of $Gd(NO_3)_3{\cdot}6H_2O$, 0.35 mmol of $Yb(NO_3)_3{\cdot}6H_2O$, and 0.035 mmol of $Er(NO_3)_3{\cdot}5H_2O$ were dissolved in 7.5 mL of deionized water to obtain a clear solution. In a separate beaker 35 mL citric acid solution (47.2 mmol) was made with deionized water. The lanthanide solution was then added dropwise into the citric acid solution under constant stirring for ~3 h. Then, 31.5 mmol of NaF was added into the previous solution. The combined mixture was then stirred for ~4 h. Subsequently, the suspension was transferred into a 100 mL Teflon-lined stainless-steel autoclave and subjected to solvothermal treatment at 200 °C for 2 h. After natural cooling, the product was separated by centrifugation, thoroughly washed with ethanol and deionized water, and finally dried at 60 °C overnight.

2.2. Electro and photoelectrochemical measurements

The electrochemical properties of the UCNPs were assessed in a standard three-electrode setup. The working electrode was fabricated by depositing the synthesized materials onto Ni foam, while a double-junction Ag/AgCl electrode and a platinum wire served as the reference and counter electrodes. All measurements were carried out in 1 M KOH. Photoelectrocatalytic OER and HER studies were performed under identical conditions with additional illumination from a simulated solar source. Linear sweep voltammetry (LSV) was recorded at 5 mV s^{-1}, and all potentials were converted to the reversible hydrogen electrode (RHE) scale. Overpotential, onset potential, and Tafel slope were extracted from the LSV curves. Turnover frequency (TOF) was estimated using cyclic voltammograms collected in the faradaic region at varying scan rates. Mass activity, electrochemically active surface area (ECSA), roughness factor (RF), and specific activity (SA) were derived from non-faradaic CV data. Catalyst durability was evaluated by a 24 h chronopotentiometric test. The detailed information is provided in the SI.

3. Result and discussion

3.1. Structural and morphological analysis

The XRD pattern of the synthesized $NaGdF_4:Yb^{3+}/Er^{3+}$ is presented in Fig. 1a. The diffraction peaks can be indexed to the (100), (110), (101), (200), (111), (201), (210), (112), (300), (211), (102), (002), (220), (202), (310), (311), (212), and (302) planes of the hexagonal β-phase $NaGdF_4$ (JCPDS card No. 27-0699).[20,22] No reflections from the cubic or α-phase were detected, confirming the exclusive formation of the hexagonal phase. The particle morphology was characterized by SEM and TEM. Fig. 1b displays the SEM image, which shows the formation of uniform hexagonal nanoparticles. TEM analysis (Fig. 1c and S1) further illustrates their well-defined geometry and sharp edges. The size distribution curve (Fig. 1d) revealed the mean size of the formed particles is 42.5 nm. High-resolution TEM was employed to probe the lattice structure, and Fig. 1e reveals clear lattice fringes. The measured interplanar distances of 0.203 and 0.228 nm correspond to the (201) and (111) planes, while a comparatively larger spacing (0.284 nm) is associated with the (101) plane of hexagonal $NaGdF_4$. These HRTEM observations align well with the XRD data, verifying the high crystallinity of the nanocrystals. The selected-area electron diffraction (SAED) pattern, shown in Fig. 1f, displays concentric diffraction rings along with distinct bright spots, indicative of the polycrystalline nature of the sample. The four most intense rings can be attributed to the (100), (110), (111), and (201) planes of β-$NaGdF_4$.

X-ray photoelectron spectroscopy (XPS) was carried out to determine the elemental composition and oxidation states of the UCNPs, and the corresponding XPS survey spectrum is presented in Fig. S2. The survey spectrum confirms the presence of Na, Gd, F, Yb, and Er. A distinct feature at 1072.4 eV corresponds to the Na 1s binding energy, which agrees well with earlier reports (Fig. 2a).[23] The signal at 142.6 eV is assigned to Gd $4d_{5/2}$, while additional peaks at 145 eV and 148.8 eV arise from Gd $4d_{3/2}$ (Fig. 2b).[13,20] The F 1s region shows two contributions: one at 684.3 eV related to F–Gd bonding and

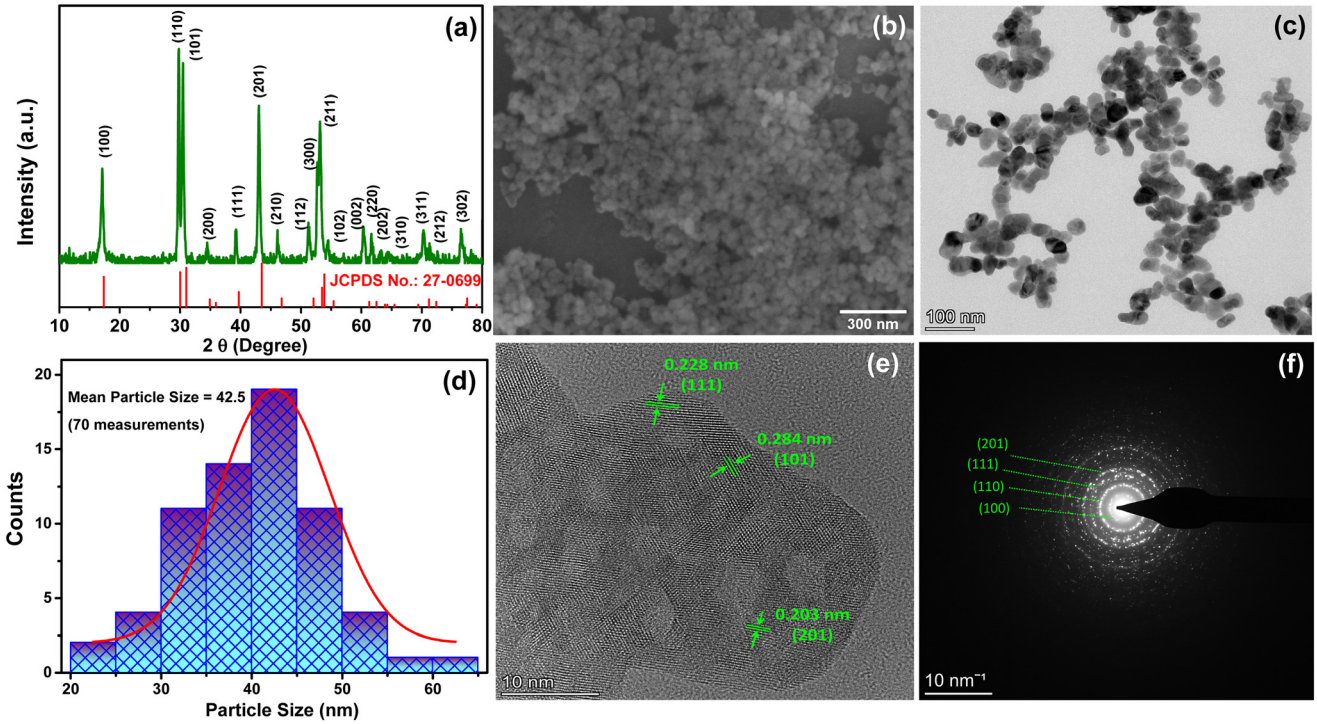

Fig. 1 (a) XRD pattern, (b) FESEM image, (c) TEM image, (d) particle size distribution curve, (e) HRTEM micrograph, and (f) SAED pattern of $NaGdF_4$: Yb^{3+}/Er^{3+}.

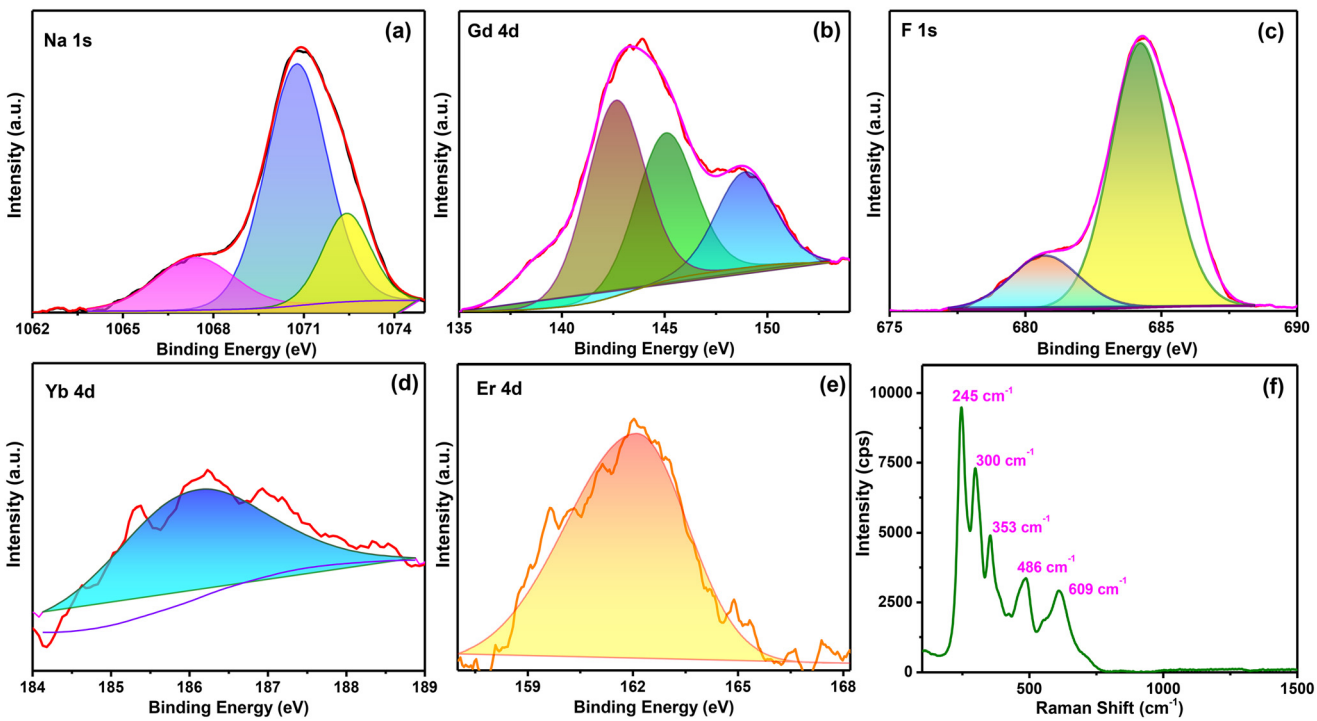

Fig. 2 High-resolution XPS spectra for (a) Na 1s, (b) Gd 4d, (c) F 1s, (d) Yb 4d, (e) Er 4d and (f) Raman spectrum of $NaGdF_4$:Yb^{3+}/Er^{3+}.

another at 680.6 eV attributed to F–C bonds (Fig. 2c).[20,24] The Yb 4d state is evident at 186.1 eV, and the peak located at 163.7 eV is associated with Er 4d, respectively (Fig. 2d and e).[24] Additionally, a feature at 835.3 eV corresponds to F KLL, while a

peak near 535.3 eV originates from Na KLL Auger transitions.[20,25] Furthermore, the EDS analysis (Fig. S3) also verifies the existence of Na, Gd, F, Yb, and Er as the elemental constituents of the synthesised material. The Raman spectrum of the UCNPs is presented in Fig. 2f, which shows five distinct peaks. As reported by Khan *et al.*, the features appearing at 245, 300, and 353 cm^{-1} correspond to lattice vibrational modes of β-$NaGdF_4$:Yb^{3+}/Er^{3+}.[22] Additional peaks located at 486 and 609 cm^{-1} arise from Na–F bond vibrations.[20,26] Collectively, all these analyses confirm that highly crystalline β-$NaGdF_4$:Yb^{3+}/Er^{3+} nanocrystals were successfully synthesized *via* the hydrothermal process.

3.2. Photoluminescence studies

The luminous intensity is a critical parameter in evaluating upconversion materials. Fig. S4 presents the photoluminescence (PL) spectrum of $NaGdF_4$:Yb^{3+}/Er^{3+}, where 980 nm near-infrared excitation generates characteristic green and red emissions. The observed peaks at 485 nm, 498 nm, and 652 nm correspond to the $^4H_{11/2} \rightarrow {}^4I_{15/2}$, $^4S_{3/2} \rightarrow {}^4I_{15/2}$, and $^4F_{9/2} \rightarrow {}^4I_{15/2}$ transitions of Er^{3+}, respectively.[27–29] The incorporation of Yb^{3+} ions plays a vital role in enhancing upconversion efficiency through Yb^{3+}-assisted energy transfer. In this mechanism, Yb^{3+} ions function as sensitizers, absorbing continuous-wave 980 nm photons to undergo a transition from the $^2F_{7/2}$ ground state to the $^2F_{5/2}$ excited state, which matches the $^4I_{11/2}$ level of Er^{3+}. The absorbed energy is subsequently transferred non-radiatively to neighbouring Er^{3+} ions, populating the $^4I_{11/2}$ state. Through a two-photon excitation pathway, these ions are further promoted to higher-lying states, namely $^2H_{11/2}$, $^4S_{3/2}$, and $^4F_{9/2}$.[30,31]

3.3. Electro and photoelectrochemical analysis

The HER activity of the synthesized materials was tested in a standard three-electrode configuration using 1 M KOH electrolyte. The polarization curves (with Ni foam included for the reference) and Tafel slopes are presented in Fig. 3a and b. For $NaGdF_4$:Yb^{3+}/Er^{3+}, the overpotentials required to achieve current densities of 10 and 25 mA cm^{-2} are 119 mV and 178 mV, respectively, with a corresponding Tafel slope of 165 mV dec^{-1}. Electrochemical impedance spectroscopy (EIS) was further employed to probe HER kinetics. The Nyquist plot (Fig. S5) displays a semicircular arc without the appearance of Warburg diffusion at lower frequencies, suggesting that mass transport does not limit the reaction and the process is dominated by charge-transfer kinetics.[1,32] Notably, the UCNP electrode exhibits a very low charge-transfer resistance (R_{ct}) value of 3.8 Ω, signifying its superior charge-transfer efficiency. The Tafel slope value of the UCNPs is greater than 120 mV dec^{-1}, indicating the hydrogen evolution on the electrode surface is likely governed by the Volmer adsorption pathway.[33] The electrocatalytic performance is closely related to the electrochemically active surface area (ECSA), which can be estimated from the double-layer capacitance (C_{dl}). The C_{dl} was derived from cyclic voltammetry (CV) measurements (Fig. 3c) recorded in the non-faradaic region between 0.22 and 0.32 V (*vs.* RHE), where the observed current originates solely from double-

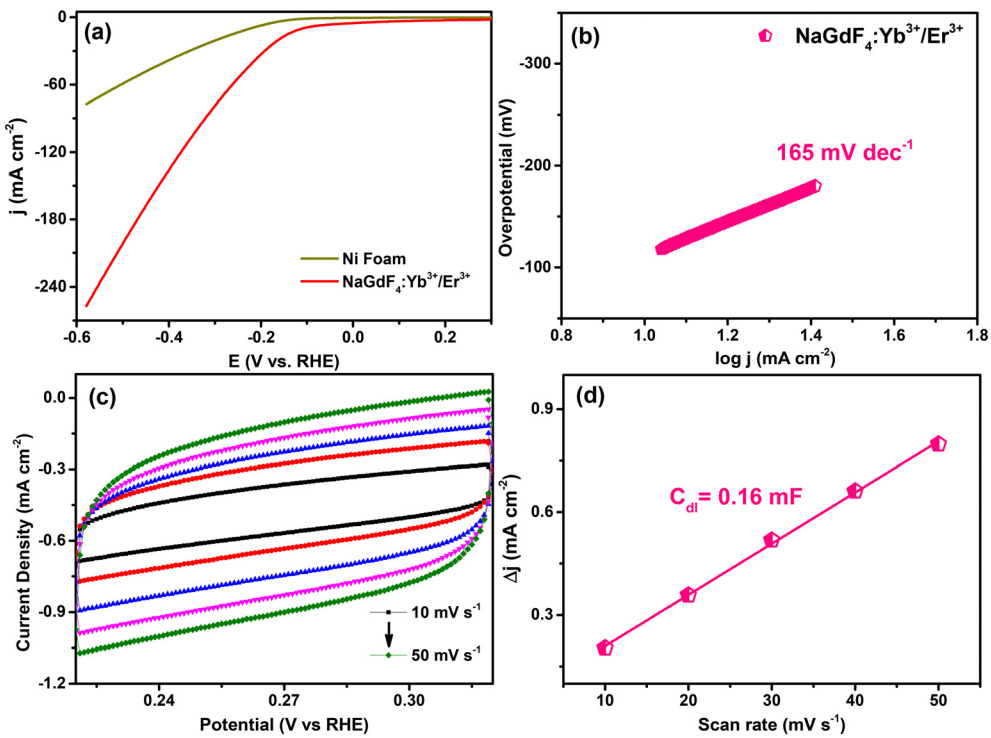

Fig. 3 (a) LSV curve (5 mV s^{-1}) for HER, (b) associated Tafel slope plot, (c) CV profiles recorded at different current densities within the non-faradaic region, and (d) plot of current density *versus* scan rate (v) for $NaGF_4$:Yb^{3+}/Er^{3+}.

layer charging. For the UCNPs, the calculated capacitance was 0.16 mF cm^{-2} (Fig. 3d), corresponding to an ECSA of 4 cm^2, suggesting a larger number of accessible catalytic active sites.[1] The UCNPs exhibited a roughness factor (RF) of 16, indicating an increased exposure of electrochemically active sites. The intrinsic catalytic performance was evaluated by calculating the exchange current density (i_{ex}) and turnover frequency (TOF) using eqn (S8) and (S6), respectively. For the HER, the synthesised UCNPs exhibit an i_{ex} and TOF corresponding to 13.5 mA cm^{-2} and 12.7 s^{-1}, respectively, confirming their superior catalytic activity.

The OER activity of the UCNPs was assessed in a three-electrode setup, where they were employed as the working electrode. As shown in the linear sweep voltammogram (Fig. 4a), the material exhibits a low onset potential of 320 mV and delivers a high current density approaching ~115 mA cm^{-2}, demonstrating excellent catalytic activity. To further probe the reaction kinetics, EIS was conducted. The Nyquist plot (Fig. S6) displays a clear semicircular profile with a R_{ct} of 10.01 Ω and an internal resistance of 3.92 Ω, derived from the *x*-axis intercept, indicating efficient charge transport within the catalyst.[34] In addition, the Tafel analysis (Fig. 4b) reveals a slope of 142 mV dec^{-1}, further supporting the favourable OER kinetics of the UCNPs. Furthermore, to assess the density of active sites involved in the OER, the ECSA was derived from the C_{dl} (Fig. 4c and d). For $NaGdF_4$:Yb^{3+}/Er^{3+}, the C_{dl} and ECSA were calculated as 0.7 mF cm^{-2} and 17.5 cm^2, respectively, indicating a substantial number of surface-active sites. The RF values, determined as 70, further suggest enhanced exposure of electrochemically active regions.[35] In addition, the intrinsic catalytic behaviour was evaluated through TOF, which reached 3.5 s^{-1}, highlighting the excellent catalytic efficiency of these UCNPs. Ensuring long-term catalytic stability is crucial for practical deployment in large-scale energy conversion. To assess this, chronopotentiometry (CP) measurements were carried out at a constant current density of 20 mA cm^{-2} for 24 h. As illustrated in Fig. S7, the potential showed negligible variation over the testing period, confirming the robust durability of the catalyst. Post-stability characterization of the catalyst was carried out to evaluate possible structural or surface changes in the catalyst after electrochemical operation. The XRD pattern remained identical to that of the fresh material (Fig. S8), indicating preservation of the crystal phase. Likewise, the XPS spectra showed no noticeable shift in the binding energies of Na, Gd, Yb, and Er, confirming the absence of phase transformation or surface reconstruction (Fig. S9). These observations demonstrate the excellent structural robustness of the catalyst. The carbon signal observed in XPS originates from the activated carbon employed during electrode fabrication rather than from any chemical modification of the material.

The photoelectrochemical hydrogen evolution performance of the synthesized UCNPs was evaluated by performing LSV under illumination and compared with measurements conducted in the absence of light. As shown in Fig. S10a, the polarization curve clearly demonstrated a pronounced enhancement in HER activity in 1 M KOH upon light exposure.

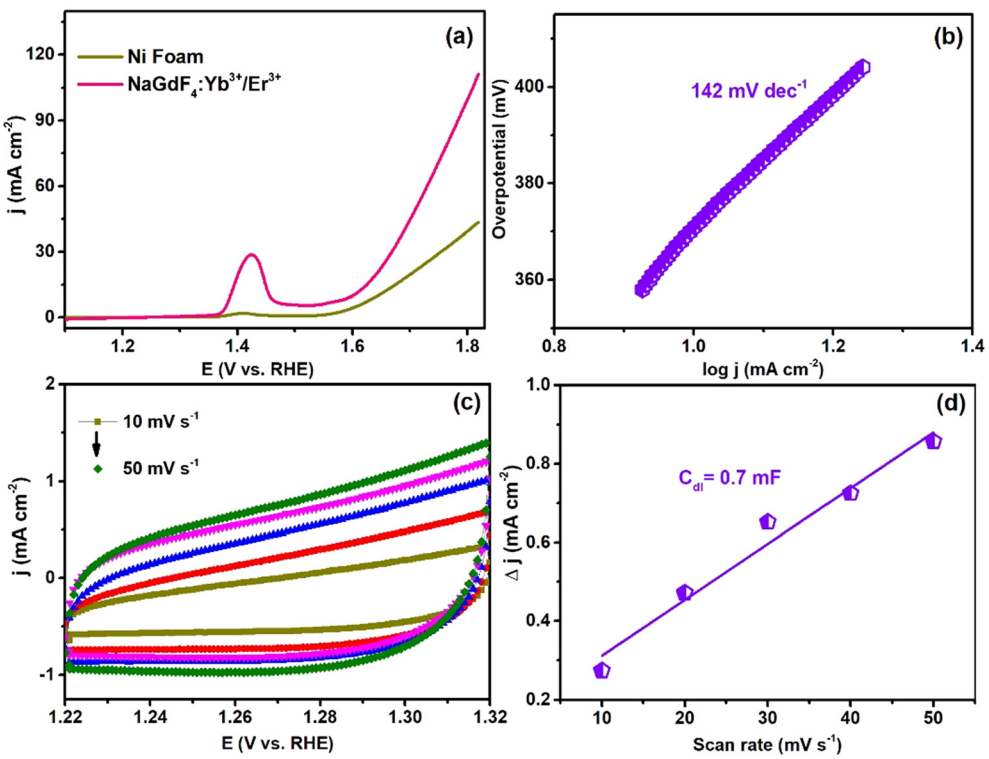

Fig. 4 (a) LSV curve (5 mV s^{-1}) for OER, (b) associated Tafel slope plot, (c) CV profiles recorded at different current densities within the non-faradaic region, and (d) plot of current density *versus* scan rate (*v*) for $NaGdF_4$:Yb^{3+}/Er^{3+}.

Due to the strong light–matter interactions under illumination, $NaGdF_4$:Yb^{3+}/Er^{3+} nanoparticles deliver markedly improved activity, achieving an overpotential of only −115 mV at 10 mA cm^{-2} and reaching a current density of −330 mA cm^{-2} at −500 mV *vs.* RHE, significantly higher than the values observed without illumination. Under illumination, the Tafel slope was found to be 79 mV dec^{-1} (Fig. S10b), showing a clear deviation from the Tafel slope found in the absence of light (165 mV dec^{-1}). This suggested that the PEC-HER catalysed by $NaGdF_4$:Yb^{3+}/Er^{3+} predominantly follows the Volmer–Heyrovsky mechanism.[36] Similarly, for the PEC-OER measurements, the polarisation profiles in Fig. S11a reveal a significant improvement in catalytic performance when the UCNPs were tested under light irradiation in 1 M KOH. Strong light–matter coupling in the presence of simulated solar light contributed to the enhanced activity, where the UCNPs achieved an onset potential of 290 mV and reached 25 mA cm^{-2} at 370 mV. These values are considerably enhanced compared to those obtained in the absence of light. Illumination also altered the reaction kinetics, with the Tafel slope decreasing to 124 mV dec^{-1} (Fig. S11b) compared to the value recorded without light (142 mV dec^{-1}). Upon light irradiation, a notable decrease in R_{ct} was observed in the case of both HER and OER (Fig. S5 and S6, Tables S1 and S2), with the UCNPs showing a reduced R_{ct} of 2.12 and 9.2 Ω, respectively, signifying enhanced charge mobility and faster ion transport under illuminated conditions. The reproducible photocurrent signals observed during successive light ON/OFF intervals (Fig. S12) indicate stable photo-induced carrier formation and more effective separation of charges. Moreover, additional electrochemical descriptors, including C_{dl}, ECSA, RF, exchange current density, and TOF (see Tables S1 and S2), further confirmed that the UCNPs displayed superior catalytic activity under photo-assisted conditions. The enhanced activity can be attributed to the UCNPs' ability to absorb NIR photons under illumination and convert them into green emission *via* the Yb^{3+}/Er^{3+} dopant system, thereby boosting their catalytic efficiency.[13,37] To ensure that the enhanced PEC activity indeed arises from the upconversion process, we compared lanthanide-doped $NaGdF_4$ with an undoped $NaGdF_4$ sample, which was synthesised under the same conditions. The undoped sample showed very limited electrochemical activity towards both OER and HER (Fig. S13), as expected for a wide band gap fluoride material, where catalysis is primarily mediated by defect sites and weak adsorption of reaction intermediates on the metal-fluoride surface.[38,39] Furthermore, the undoped $NaGdF_4$ also showed significantly lower PEC activity (Fig. S14). This result suggests that the enhanced activity is due to the combined effects of NIR-assisted light harvesting and the redox sites introduced by Yb^{3+}/Er^{3+} ionic pair. The Yb^{3+}/Er^{3+} ions act as a sensitiser–

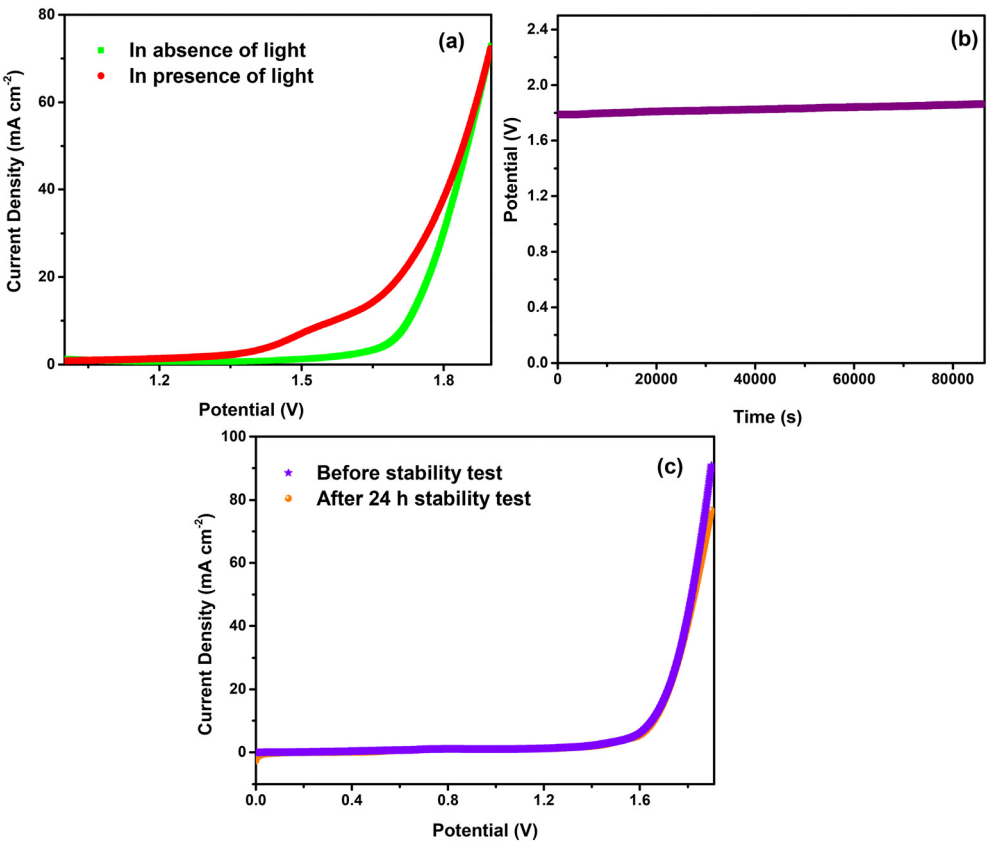

Fig. 5 (a) LSV profiles of the $NaGdF_4$:Yb^{3+}/Er^{3+}||$NaGdF_4$:Yb^{3+}/Er^{3+} cell in 1.0 M KOH, (b) chronopotentiometry curve for overall water splitting for 24 h, and (c) LSV comparison of $NaGdF_4$:Yb^{3+}/Er^{3+} before and after the 24 h durability test.

activator pair, where they absorb near-infrared photons and emit visible light through a multi-step energy transfer process (as shown in Fig. S15),[40,41] thus effectively enhancing the photon energy available at the catalyst surface and facilitating charge excitation.[42–44]

For evaluating overall water splitting, a two-electrode setup was assembled with the synthesised catalysts serving as both anode and cathode. As presented in Fig. 5a, the $NaGdF_4$:Yb^{3+}/Er^{3+}||$NaGdF_4$:Yb^{3+}/Er^{3+} system demonstrated excellent performance in 1.0 M KOH, requiring ~1.72 V to achieve 10 mA cm^{-2}. Stability assessment at a fixed current density of 25 mA cm^{-2} over 24 h (Fig. 5b) revealed consistent voltage retention, with the cell operating at ~1.7–1.8 V throughout the test duration. Furthermore, the LSV curves recorded before and after durability testing exhibited negligible loss in water oxidation activity (Fig. 5c). The overall water splitting experiments were conducted using the $NaGdF_4$:Yb^{3+}/Er^{3+}||$NaGdF_4$:Yb^{3+}/Er^{3+} device under simulated solar irradiation, where the system required only ~1.52 V to deliver a current density of 10 mA cm^{-2} (Fig. 4a), which is on par with several electrolyzers documented in literature.[2,4,45–48] This underscores the potential of the prepared material for practical solar-driven water splitting.

4. Conclusion

In summary, β-$NaGdF_4$:Yb^{3+}/Er^{3+} upconversion nanoparticles were successfully synthesized and demonstrated as a versatile bifunctional catalyst for both electrochemical and photoelectrochemical water splitting. Their unique upconversion properties enable effective utilization of the near-infrared region of the solar spectrum, resulting in significantly enhanced PEC performance. The catalyst exhibits low overpotentials, excellent charge-transfer efficiency, and remarkable stability during long-term operation, highlighting its promise as a cost-effective and durable alternative to noble-metal-based systems. The ability of $NaGdF_4$:Yb^{3+}/Er^{3+} to function as both HER and OER catalyst and to drive overall water splitting under solar irradiation establishes an alternative paradigm for multifunctional UCNP-based catalysts. Future work will focus on coupling these UCNPs with complementary visible-light semiconductors and optimizing their surface chemistry to further maximise solar energy conversion and hydrogen generation efficiency.

Author contributions

Soumantika: investigation, formal analysis. Debika: formal analysis, data curation, writing of the manuscript. Neha: formal analysis. Bo-Yan: formal analysis. Jeffrey Wu: writing – review & editing. Rakesh Sharma: writing – review & editing, supervision, conceptualization.

Conflicts of interest

The authors have no competing interests to disclose.

Data availability

The data supporting this article have been included as part of the supplementary information (SI). Supplementary information: chemicals used, characterization of the synthesized materials and instrument details, electrode preparation, equations used, figures/tables supporting the manuscript. See DOI: https://doi.org/10.1039/d5lf00409h.

Acknowledgements

The authors gratefully acknowledge the CRF, IIT Jodhpur, and National Taiwan University for providing the necessary facilities for material characterization. Financial support from the INDO-TAIWAN research grant, India (Grant No.: 2024/IN-TW/04) is also duly recognized.

References

1 Z. Zhao, F. Qin, S. Kasiraju, L. Xie, M. K. Alam, S. Chen, D. Wang, Z. Ren, Z. Wang, L. C. Grabow and J. Bao, *ACS Catal.*, 2017, **7**, 7312–7318.
2 H. Qin, P. Xu, S. Lu, Y. Wang, J. Ying, T. Liu, M. Guo, W. Huang, Q. Shen and Z. Yu, *J. Power Sources*, 2025, **633**, 236398.
3 Q. Shi, Q. Liu, Y. Ma, Z. Fang, Z. Liang, G. Shao, B. Tang, W. Yang, L. Qin and X. Fang, *Adv. Energy Mater.*, 2020, **10**, 1903854.
4 U. Farooq and T. Ahmad, *Int. J. Hydrogen Energy*, 2024, **64**, 290–300.
5 H. Khan, S. E. Lofland, K. V. Ramanujachary, N. Alhokbany and T. Ahmad, *ACS Appl. Energy Mater.*, 2023, **6**, 8102–8110.
6 Z. Huang, J. Zhang, M. Humayun, Y. Liu, W. Xiao, C. Feng, K. Zhao, B. Wu, Y. Fu, M. Bououdina, H. Zhang, G. Chen and C. Wang, *J. Energy Chem.*, 2025, **111**, 94–108.
7 B. Chen, M. Humayun, Y. Li, H. Zhang, H. Sun, Y. Wu and C. Wang, *ACS Sustainable Chem. Eng.*, 2021, **9**, 14180–14192.
8 L. Yao, H. Zhang, M. Humayun, Y. Fu, X. Xu, C. Feng and C. Wang, *J. Alloys Compd.*, 2023, **936**, 168206.
9 A. Mehtab and T. Ahmad, *ACS Catal.*, 2024, **14**, 691–702.
10 R. Saini, F. Naaz, A. H. Bashal, A. H. Pandit and U. Farooq, *Green Chem.*, 2024, **26**, 57–102.
11 F. Naaz, U. Farooq, M. A. M. Khan and T. Ahmad, *ACS Omega*, 2020, **5**, 26063–26076.
12 A. Mehtab, S. A. Ali, P. P. Ingole, Y. Mao, S. M. Alshehri and T. Ahmad, *ACS Appl. Energy Mater.*, 2023, **6**, 12003–12012.
13 G. Wu, J. Xue, D. Lei, Y. Zhou, Z. Cao, K. Ren, Q. Bi and Z. Leng, *Appl. Surf. Sci.*, 2024, **664**, 160248.
14 F. Wang, R. Deng and X. Liu, *Nat. Protoc.*, 2014, **9**, 1634–1644.
15 J. Zhang, Y. Huang, L. Jin, F. Rosei, F. Vetrone and J. P. Claverie, *ACS Appl. Mater. Interfaces*, 2017, **9**, 8142–8150.
16 Y. Chen, S. Mishra, G. Ledoux, E. Jeanneau, M. Daniel, J. Zhang and S. Daniele, *Chem. – Asian J.*, 2014, **9**, 2415–2421.
17 Z. Qiu, J. Shu and D. Tang, *Anal. Chem.*, 2018, **90**, 1021–1028.
18 N. Prakash, D. Thangaraju, R. Karthikeyan, M. Arivanandhan, Y. Shimura and Y. Hayakawa, *RSC Adv.*, 2016, **6**, 80655–80665.

19 H. Anwer and J.-W. Park, *Appl. Catal., B*, 2019, **243**, 438–447.
20 L. Ma, T. Chen, Q. Li, M. Mai, X. Ye, J. Mai, C. Liu, J. Zhang, D. Lin and X. Ma, *Appl. Surf. Sci.*, 2022, **585**, 152650.
21 R. Yi, C. Zhang, D. Shan, M. Di, C. Li, Y. Wang, Y. Wu, J. Zheng, W. Liu and B. Wang, *View*, 2025, **6**, 20240131.
22 L. U. Khan, Z. U. Khan, R. V. Rodrigues, L. S. da Costa, M. Gidlund and H. F. Brito, *J. Mater. Sci.: Mater. Electron.*, 2019, **30**, 16856–16863.
23 K. Lingeshwar Reddy, V. Srinivas, K. R. Shankar, S. Kumar, V. Sharma, A. Kumar, A. Bahuguna, K. Bhattacharyya and V. Krishnan, *J. Phys. Chem. C*, 2017, **121**, 11783–11793.
24 P. Ramasamy, P. Chandra, S. W. Rhee and J. Kim, *Nanoscale*, 2013, **5**, 8711–8717.
25 M. Liu, Z. Shi, X. Wang, Y. Zhang, X. Mo, R. Jiang, Z. Liu, L. Fan, C.-g. Ma and F. Shi, *Nanoscale*, 2018, **10**, 20279–20288.
26 S. Yamini, M. Gunaseelan, G. A. Kumar, S. Singh, G. C. Dannangoda, K. S. Martirosyan, D. K. Sardar, S. Sivakumar, A. Girigoswami and J. Senthilselvan, *Microchim. Acta*, 2020, **187**, 317.
27 Y. Liu, D. Tu, H. Zhu, R. Li, W. Luo and X. Chen, *Adv. Mater.*, 2010, **22**, 3266–3271.
28 X. Li, Y. Li, D. Jia, G. Hu, D. Zhang, S. Jin and M. Wang, *Opt. Mater.*, 2025, **162**, 116812.
29 J. Méndez-Ramos, J. C. Ruiz-Morales, P. Acosta-Mora, J. del-Castillo and A. C. Yanes, *J. Power Sources*, 2013, **238**, 313–317.
30 C. Liao, J. Wang, H. Liu, J. Xu, W. Zhou, P. Guo, T. Wang, G. Zhou and J. Hu, *Ceram. Int.*, 2025, **51**, 16986–16995.
31 N. Ren, Z. Feng, N. Liang, J. Xie, A. Wang, C. Sun and X. Yu, *Mater. Sci. Eng., C*, 2020, **111**, 110827.
32 D. Merki, H. Vrubel, L. Rovelli, S. Fierro and X. Hu, *Chem. Sci.*, 2012, **3**, 2515–2525.
33 K. P. Akshay Kumar, O. Alduhaish and M. Pumera, *Electrochem. Commun.*, 2021, **125**, 106977.
34 S. Chen and S.-Z. Qiao, *ACS Nano*, 2013, **7**, 10190–10196.
35 D. Gogoi, R. S. Karmur, M. R. Das and N. N. Ghosh, *J. Mater. Chem. A*, 2023, **11**, 23867–23880.
36 R. S. Karmur, D. A. Upar, Z. Mei, D. Hao, C. Liu and N. N. Ghosh, *Energy Fuels*, 2025, **39**, 2854–2866.
37 K. Feng, Z. Cai, D. Huang, L. Li, K. Wang, Y. Li, C. Wang, J. Song, L. Zhao, W. Wei and F. Jiang, *Sustainable Energy Fuels*, 2020, **4**, 2669–2674.
38 Z. Luo, *J. Mater. Chem. A*, 2025, **13**, 2537–2573.
39 K. Lemoine, J. Lhoste, A. Hémon-Ribaud, N. Heidary, V. Maisonneuve, A. Guiet and N. Kornienko, *Chem. Sci.*, 2019, **10**, 9209–9218.
40 M. Quintanilla, E. Hemmer, J. Marques-Hueso, S. Rohani, G. Lucchini, M. Wang, R. R. Zamani, V. Roddatis, A. Speghini, B. S. Richards and F. Vetrone, *Nanoscale*, 2022, **14**, 1492–1504.
41 Y. Shi, F. Zhang, J. Xu, K. Zhou, C. Chen, J. Cheng and P. Li, *J. Mater. Sci.*, 2019, **54**, 8461–8471.
42 F. Auzel, *Chem. Rev.*, 2004, **104**, 139–174.
43 D. Gogoi, S. Jana, N. Patel, B.-Y. Feng, J. C. S. Wu and R. K. Sharma, *Chem. Commun.*, 2026, **62**, 2942–2946.
44 X. Cheng, D. Tu, W. Zheng and X. Chen, *Chem. Commun.*, 2020, **56**, 15118–15132.
45 Y. Wang, S. Wang, Z.-L. Ma, L.-T. Yan, X.-B. Zhao, Y.-Y. Xue, J.-M. Huo, X. Yuan, S.-N. Li and Q.-G. Zhai, *Adv. Mater.*, 2022, **34**, 2107488.
46 M. Zhao, W. Li, J. Li, W. Hu and C. M. Li, *Adv. Sci.*, 2020, **7**, 2001965.
47 P. Zhai, M. Xia, Y. Wu, G. Zhang, J. Gao, B. Zhang, S. Cao, Y. Zhang, Z. Li, Z. Fan, C. Wang, X. Zhang, J. T. Miller, L. Sun and J. Hou, *Nat. Commun.*, 2021, **12**, 4587.
48 G. Chen, T. Wang, J. Zhang, P. Liu, H. Sun, X. Zhuang, M. Chen and X. Feng, *Adv. Mater.*, 2018, **30**, 1706279.